GEOPHYSICS, VOL. 87, NO. 5 (SEPTEMBER-OCTOBER 2022); P. IM177–IM188, 12 FIGS.
10.1190/GEO2021-0662.1

Toward accurate seismic flattening: Methods and applications

Xinming Wu[1], Yaxing Li[1], and Paphop Sawasdee[2]

ABSTRACT

Seismic flattening maps a seismic volume from the original space in depth (or two-way traveltime) to the Wheeler domain in geologic time where all of the seismic reflections are horizontally aligned. It provides an efficient way to interpret a whole volume of horizons all at once by extracting the horizontal slices in the flattened space. Conventional slope-based flattening methods that can locally flatten the seismic reflections, however, often fail to flatten the reflections in a global sense and cannot accurately align the reflections across faults. We have developed an iterative method to improve the flattening by using the slopes and correlations of seismic traces. The local slopes, estimated for each image sample, can locally follow reflections but may fail to track the reflections over a long distance or correlate the reflections across faults. The seismic correlations, computed for randomly and sparsely extracted seismic traces, help to align the corresponding reflections over a long distance and across faults. We compute flattening shifts, one for each image sample, by fitting the seismic slopes and correlating in the least-squares sense. We further apply the shifts to relatively adjust the seismic samples in the vertical direction so that all of the reflections are horizontally aligned. We iteratively flatten the seismic volume by repeating the process multiple times (often less than five times). With the flattening shifts, we can compute a relative geologic time (RGT) volume that implicitly contains all the structure information of the seismic volume. An arbitrary number of horizons then can be extracted as isosurfaces of RGT values. Multiple field examples demonstrate that our method significantly improves the flattening, especially across faults and missing data zones, compared with conventional flattening methods. Our method is especially helpful to interpret subtle stratigraphic features (e.g., vertically thin channels) by providing an accurately flattened seismic volume.

INTRODUCTION

The Wheeler diagram (Wheeler, 1958), or the Wheeler volume in three dimensions, generated from a seismic image, presents a chronostratigraphic section (Vail et al., 1977) for seismic stratigraphic interpretation. Seismic flattening is a volumetric method to map a seismic volume from the original space to the Wheeler domain (Qayyum et al., 2017, 2018). Seismic flattening can be achieved by multiple types of methods such as horizon-based, unit-vector-transform (UVT), phase-unwrapping, and slope-based ones.

In the horizon-based flattening methods, Zeng et al. (1998a, 1998b) propose to use some manually interpreted seismic horizons to first compute a "stratal time volume" and further use it to map the corresponding seismic volume to a "stratal slice volume" in the flattened space. De Groot et al. (2010) and Qayyum et al. (2012) propose to use "horizon cubes" with high-density horizons to improve the accuracy of the horizon-based flattening. Dorn (2011, 2013) introduces interpreted unconformities and faulted horizons, respectively, to deal with vertical unconformity gaps and lateral faulting gaps during the flattening.

In the UVT-transform method, Mallet (2004, 2014) proposes a mathematically general framework of generating a "GeoChron" model or flattening a seismic volume. Based on the framework of UVT transform, Labrunye et al. (2009) and Mallet et al. (2010) propose feasible ways to flatten a seismic volume with folding and faulting structures, whereas Mallet (2014) and Labrunye and Carn (2015) propose a way to deal with unconformities in flattening a seismic volume.

In the phase-unwrapping methods, Stark (2003, 2004, 2005) proposes to unwrap seismic instantaneous phases to first compute a

Manuscript received by the Editor 7 October 2021; revised manuscript received 10 May 2022; published ahead of production 24 May 2022; published online 13 July 2022.
[1]University of Science and Technology of China, School of Earth and Space Sciences, Hefei, China. E-mail: xinmwu@ustc.edu.cn (corresponding author); yxli2017@mail.ustc.edu.cn.
[2]PTT Exploration and Production PLC, Bangkok, Thailand. E-mail: paphops@pttep.com.

DOI:10.1190/geo2021-0662.1

relative geologic time (RGT) volume and then use it to flatten the seismic volume. Wu and Zhong (2012) improve the phase-unwrapping method by introducing the constraints of interpreted unconformities and horizons.

In the slope-based methods, Bienati and Spagnolini (2001) and Lomask et al. (2006) propose to iteratively flatten a seismic volume, where the vertical flattening shifts are computed by fitting the seismic slopes in the least-squares sense at each iteration. Parks (2010) improves the efficiency of the slope-based flattening method by solving a linear system with slopes. Fomel (2010) proposes to flatten a seismic volume by predictive painting with seismic slopes. Luo and Hale (2013) propose to undo the faulting and folding in the seismic volume and therefore obtain a flattened volume by using the vector shifts that are computed with fault throws and seismic normal vectors (or slopes). The slope-based methods are widely used but require undoing faulting (Luo and Hale, 2013) before flattening or introducing constraints on the opposite sides of faults (Wu and Hale, 2015) to align reflections across the faults in flattening a seismic volume with faults. Similarly, Xue et al. (2018) propose to track horizons across faults with fault-slip vectors that are precomputed by correlating reflections across the faults. In addition, the flattening method with only local slopes may fail to accurately align a seismic reflection over a long distance due to possible error propagations.

In this paper, we improve the slope-based flattening by using the seismic correlations and the local slopes. We estimate the slopes, an inline and crossline slope for each image sample, by using structure tensors (Bakker, 2002; Fehmers and Höcker, 2003; Hale, 2009). The estimated slopes can locally follow seismic reflections but often fail to consistently track the reflections over a long distance and cannot correlate the reflections across faults. We calculate the correlations of seismic traces that are randomly and sparsely extracted from the seismic volume. We compute flattening shifts by fitting the local slopes and seismic correlations in the least-squares sense. The correlation of the traces on the opposite sides of a fault is helpful to align reflections across the fault. In addition, the correlation of traces away from each other is helpful to correct possible error propagations and align reflections globally. We perform our flattening method iteratively, where the local slopes and correlations are recomputed at each iteration from the previously flattened volume. From the final flattening shifts, we can further compute an RGT volume and extract a whole volume of seismic horizons all at once. We apply our method to multiple 2D and 3D field examples that are complicated by faults and complex folding structures. The flattening results demonstrate that our method is significantly superior to the conventional slope-based method in aligning the seismic reflections globally and across faults. Two field examples with rich channels illustrate that our method is especially helpful to interpret vertically thin channels (with a thickness of only one or two vertical sampling rates) by providing a perfectly flattened volume.

IMPROVED SEISMIC FLATTENING

To flatten a seismic image, conventional flattening methods are attempting to warp the seismic image from the original space to a new space with flat reflections by using the vertical (Lomask et al., 2006; Parks, 2010) or nonvertical shifts (Luo and Hale, 2013). These flattening shifts are computed for each seismic image sample by solving the partial differential equations (PDEs) that are constructed with local seismic slopes or normal vectors. We improve the flattening method with vertical shifts by introducing the constraints of seismic trace correlations to compute the shifts so that it can flatten a seismic image in a more global sense and more accurately align reflections across faults.

Conventional flattening with vertical shifts

In the flattening methods with vertical shifts, Parks (2010) proposes to solve a set of linear PDEs for the shifts $s(x,y,z)$ in the original space of depth z and then convert them to the RGT (τ) space $s(x,y,\tau)$ that will flatten the seismic image. The linear PDEs for 3D flattening are constructed with local seismic slopes as follows:

$$\begin{bmatrix} w(x,y,z)\left(-\frac{\partial s}{\partial x}-p(x,y,z)\frac{\partial s}{\partial z}\right) \\ w(x,y,z)\left(-\frac{\partial s}{\partial y}-q(x,y,z)\frac{\partial s}{\partial z}\right) \\ \mu\frac{\partial s}{\partial z} \end{bmatrix} \approx \begin{bmatrix} w(x,y,z)p(x,y,z) \\ w(x,y,z)q(x,y,z) \\ 0 \end{bmatrix}, \quad (1)$$

where $p(x,y,z)$ and $q(x,y,z)$, respectively, are the inline and crossline reflection slopes that can be estimated from the 3D seismic image by using the structure tensors (Bakker et al., 1999; Bakker, 2002; Hale, 2009), plane-wave destruction (Fomel, 2002), semblance scanning (Marfurt, 2006), and log-Gabor filtering (Yu et al., 2013). In equation 1, $w(x,y,z) \in [0,1]$ is a weighting map that measures the quality of the estimated slopes. For example, we may define $w(x,y,z)$ as a coherence map because the slope estimation is typically poor in the area where the coherence of seismic reflections is low. The third equation is a regularization term to impose vertical smoothness on the shifts to be computed, and μ is a small constant ($\mu = 0.01$), which balances the regularization term and the flattening equations.

By solving these PDEs in the least-squares sense, we are able to compute the shifts $s(x,y,z)$ in the original depth space z. These shifts map the seismic image samples from the original space (x,y,z) to the flattened space in the RGT $\tau(x,y,z) = z + s(x,y,z)$. Assuming that $\tau(x,y,z)$ monotonically increases in the vertical direction, we can use an inverse interpolation (Parks, 2010) to convert the shifts (computed in the original depth space) to the RGT space $s(x,y,\tau)$ which will map the seismic image to the grid in the flattened space.

We test this conventional flattening method on a 2D field seismic image in Figure 1a that is complicated by faults. We solve the flattening equation 1 with the local slopes in Figure 1b and compute a flattened image in Figure 1c. We observe that this method locally flattens the seismic reflections but fails to flatten the reflections in a global sense and cannot accurately align the reflections across faults (such as the one denoted by the yellow line). This is because the local slopes, used for flattening, can locally follow reflections but typically fail to track the reflections over a long distance and cannot correlate the reflections across faults.

Improved flattening with correlations

Inspired by the idea of using seismic waveform correlations for extracting individual horizons (Wu and Fomel, 2018), we improve the flattening by introducing the pairwise correlations of seismic traces into equation 1 for computing the flattening shifts. Although the individual horizon picking and flattening use the same information of local slopes and multigrid correlations, the flattening shows some advantages in computing seismic horizons. First, the individual horizon picking fits the correlations within a vertically local

window centered at an initial horizon, and the initial needs to be sufficiently good so that the target horizon will be included within the local window. Second, picking a horizon individually ignores the consistency constraints among the horizons or structures above and below, which may yield geologically unreasonable picking results (e.g., intersecting horizons). However, the flattening method

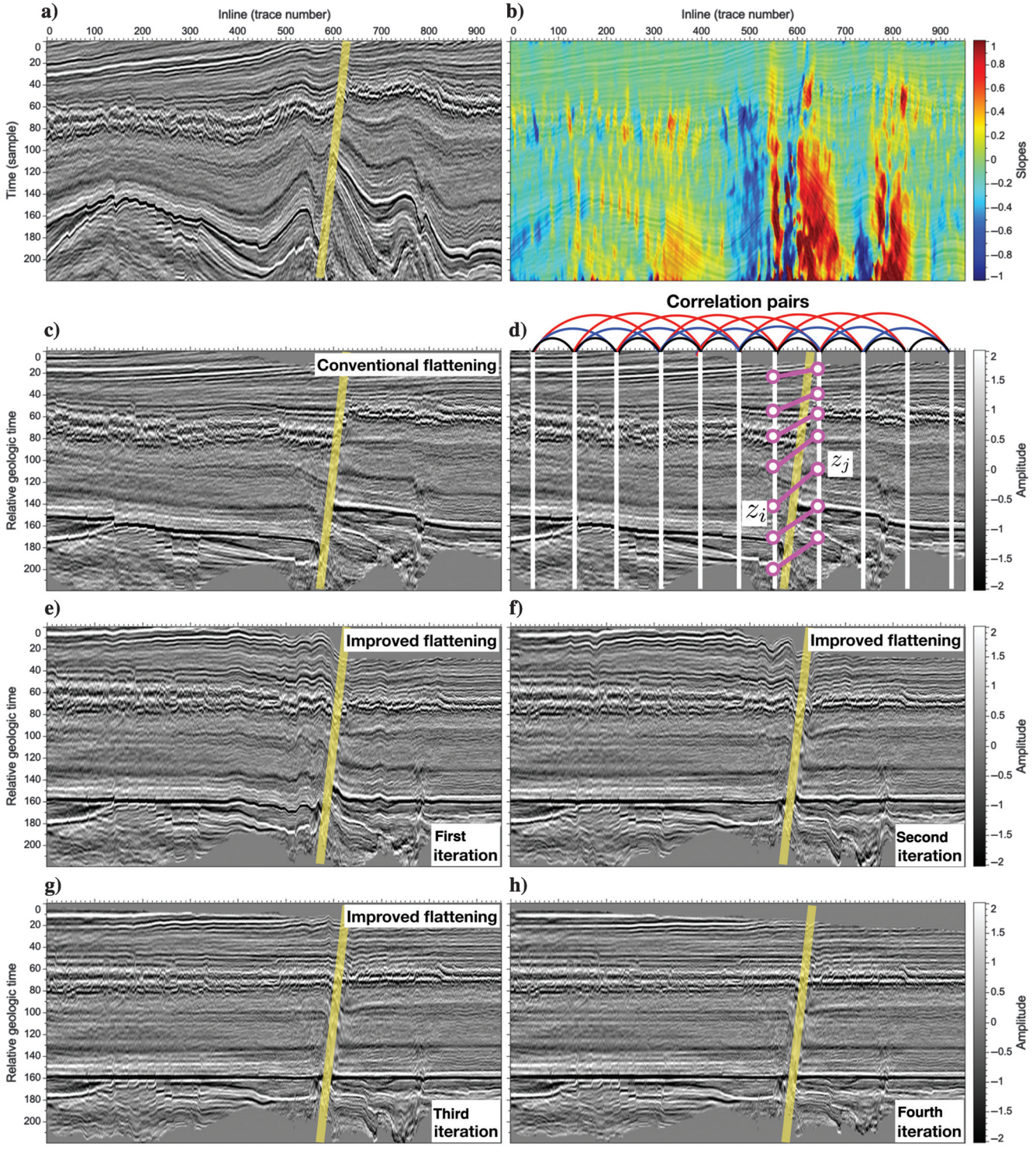

Figure 1. For (a) a seismic image complicated by faults, (b) the conventional flattening method using only reflection slopes cannot accurately (c) flatten the seismic image, especially near the faults (such as the one denoted by the yellow line). We propose (d) an improved flattening method with seismic slopes and seismic correlations, which (e–h) iteratively updates the flattening until (h) all of the seismic reflections are horizontally aligned at the fourth iteration. Note that fault information is not used in the flattening.

DOI:10.1190/geo2021-0662.1

DOI:10.1190/geo2021-0662.1

simultaneously computes all the horizons that globally fit the correlations of seismic traces in the entire vertical domain. In addition, prior regularizations can be easily imposed on the flattening to maintain the consistency among horizons.

The black, blue, and red curves on the top of Figure 1d denote the pairwise correlations of seismic traces with different lateral gaps. The correlations of traces with large gaps are helpful to align reflections globally, and the correlations of traces on the opposite sides of a fault are helpful to align reflections across the fault. After computing the pairwise correlations of the ith and jth traces by using the dynamic time warping algorithm (Hale, 2013), we are able to find many pairs of corresponding depths such as the correlated points z_i and z_j denoted by magenta circles in Figure 1d. As these corresponding depths are expected to be horizontally aligned in the flattening, we can construct the following equations for the flattening shifts:

$$s(z_i) - s(z_j) = z_j - z_i. \tag{2}$$

This equation aims to compute shifts that relatively shift the correlated points to the same depth.

After integrating these equations from correlations, we compute the flattening shifts that fit the local slopes and seismic correlations by solving the least-squares solution of the following equations:

$$\begin{bmatrix} w(x,y,z)\left(-\frac{\partial s}{\partial x} - p(x,y,z)\frac{\partial s}{\partial z}\right) \\ w(x,y,z)\left(-\frac{\partial s}{\partial y} - q(x,y,z)\frac{\partial s}{\partial z}\right) \\ \lambda(s(z_i) - s(z_j)) \\ \mu\frac{\partial s}{\partial z} \end{bmatrix} \approx \begin{bmatrix} w(x,y,z)p(x,y,z) \\ w(x,y,z)q(x,y,z) \\ \lambda(z_j - z_i) \\ 0 \end{bmatrix}, \tag{3}$$

where λ is a constant number providing a trade-off between fitting the local slopes and global correlations. We set $\lambda = 0.001$ for all the examples in this paper. Note that the third term from correlations represents a large set of $M \times N$ equations, where M represents the number of pairs of correlated traces and N represents the number of samples in a trace. Then, the last equation is a regularization term to impose vertical smoothness on the shifts. We compute the least-squares solution to equation 3 by solving the corresponding normal equation which is a large 3D linear system. We solve the linear system iteratively by using the conjugate-gradient method which allows us to avoid explicitly forming the large matrices for the linear system.

In computing the pairwise correlations, the pairs of ith and jth traces are randomly extracted at the lateral grid of the seismic image to be flattened. In three dimensions, each pair of traces is extracted at a random inline and crossline index. Theoretically, we could compute all possible pairs of seismic correlations and include all the correlations in the flattening equations, but it is computationally expensive to compute numerous pairwise correlations and solve a huge linear system in equation 3. To save computational cost, we compute only a subset of the pairwise correlations where the distance between ith and jth traces is in a predefined range (e.g., $[5, 120]$) and the randomly extracted traces are approximately evenly distributed in space.

In the practical flattening process, we notice that we may need to iteratively apply our improved flattening method multiple times to obtain an accurately flattened image. We stop the iteration when the flattening shifts, computed at the latest iteration, are close to zero. From our experience, the flattening shifts typically converge in less than five iterations. As an example in Figure 1, we iteratively apply our method to a previously flattened image and obtain a finally flattened image at the fourth iteration as shown in Figure 1h. At each iteration, the local slopes and correlations for computing flattening shifts are recalculated from the previously flattened image. As the correlation traces are randomly extracted, the traces to be correlated at each iteration are all different, which is helpful to introduce more correlation constraints into the whole flattening process.

By using our improved flattening method with correlations and local slopes, the final flattened result (Figure 1h) is significantly improved from the one (Figure 1c) using the conventional method with only slopes. Most of the reflections in Figure 1h are perfectly horizontally aligned in the whole lateral space. Moreover, our method can accurately flatten the reflections across faults without the need to interpret the faults.

There is a trade-off between the flattening efficiency and accuracy in selecting the number of traces to be correlated. Obviously, correlating all possible pairs of seismic traces for the flattening would be computationally exhausting due to the cost of computing the correlations and solving large linear systems (equation 3) with numerous correlation equations. Therefore, we compute correlations of seismic traces on a lateral sparse grid. To explore how many pairs of traces should be correlated, we run some numerical experiments shown in Figure 2. In these experiments, the 2D seismic image (Figure 1a) is flattened by using our method with correlations of every 5 traces (Figure 2a), 10 traces (Figure 2b), 15 traces (Figure 2c), 20 traces (Figure 2d), 30 traces (Figure 2e), 40 traces (Figure 2f), 50 traces (Figure 2g), and 60 traces (Figure 2h), respectively. We observe that calculating pairwise correlations of seismic traces on a sparse grid of every 5, 10, or 15 traces is sufficient to obtain a well-flattened result. Note that we also set a threshold of the largest distance to further reduce the number of pairwise correlations. For example, on a sparse grid of every five traces, we only compute the pairwise correlations when the lateral distance between the pair of traces is less than 120 traces. In this way, flattening with the correlations of traces on the sparse grids of every 5 and 10 traces would be computationally affordable. Another important point is that the sparse grid is redefined (by choosing different starting traces in inline and crossline directions) at each flattening iteration, which helps to include more correlation constraints into the flattening.

RGT AND HORIZON EXTRACTION

The flattening process with vertical shifts is basically mapping the seismic image from the original space in depth (x, y, z) to the RGT space (x, y, τ) where all of the reflections are horizontally aligned. The corresponding RGT map $\tau(x, y, z)$ can be computed from the flattening shifts as

$$\tau(x, y, z) = z + s(x, y, z). \tag{4}$$

Figure 3a and 3b shows the RGT maps computed from the vertical shifts of the conventional and our improved flattening methods, respectively.

Such an RGT map can be considered as a model that implicitly contains all the structural and stratigraphic information of the corresponding seismic image. For example, contours or

isocurves of the RGT map correspond to geologically synchronous horizons. The lateral discontinuities of the RGT map indicate the positions of faults and the dislocations of the RGT contours across faults represent the fault displacements. The color-shaded curves in Figure 3c and 3d are contours extracted from the corresponding RGT maps in Figure 3a and 3b, respectively. With an accurate RGT map in Figure 3b computed with our improved flattening method, the extracted RGT contours accurately follow the horizons in the whole seismic image even across faults as shown in Figure 3d. Mathematically, we are able

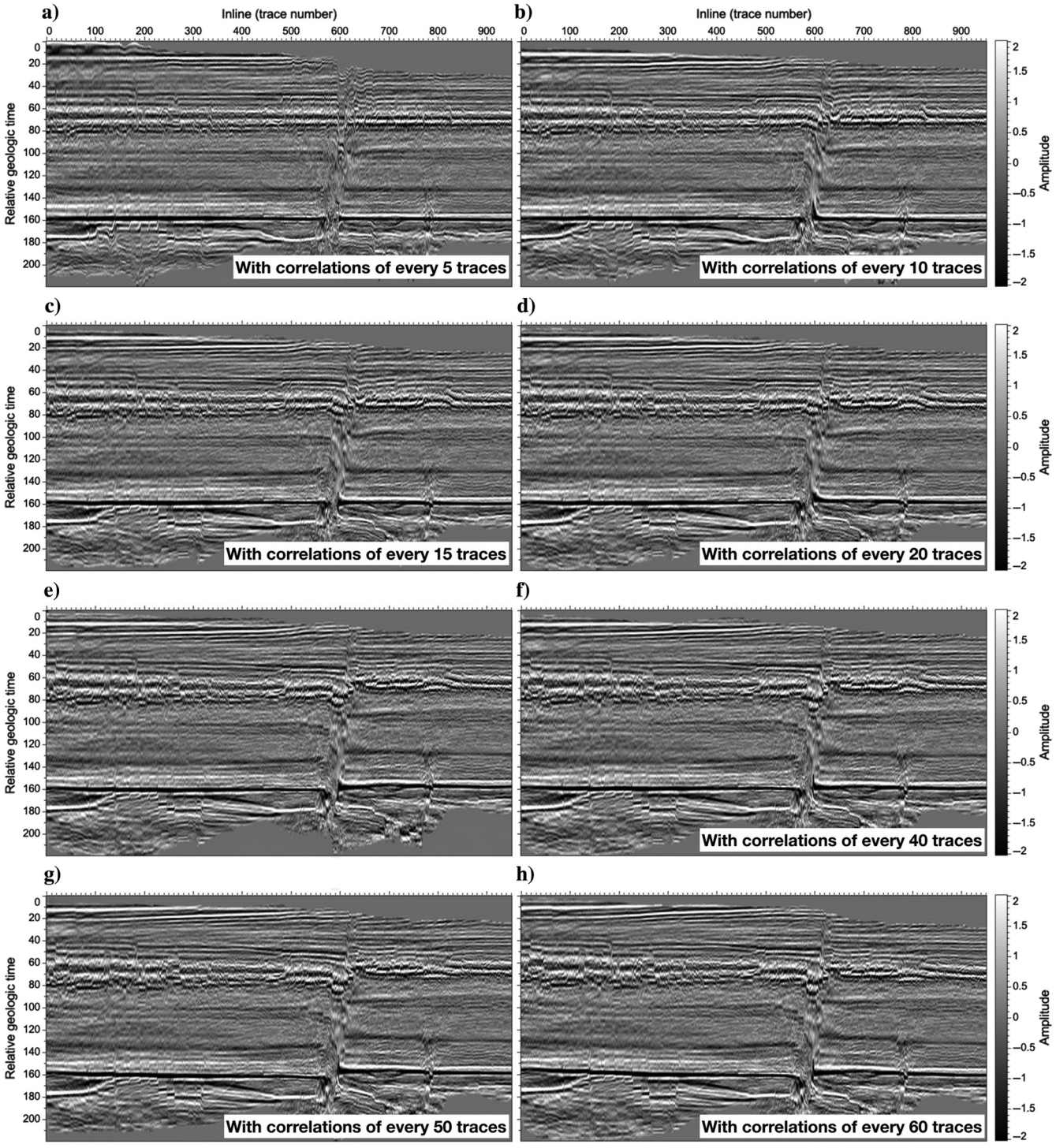

Figure 2. Flattening results with correlations of every (a) 5 traces, (b) 10 traces, (c) 15 traces, (d) 20 traces, (e) 30 traces, (f) 40 traces, (g) 50 traces, and (h) 60 traces, respectively. We observe that using the constraints of more seismic correlations yields better flattened results.

DOI:10.1190/geo2021-0662.1

to extract any horizon $z(x, y, \tau)$ at an expected RGT τ from the RGT map $\tau(x, y, z)$ by using an inverse interpolation (Parks, 2010) where we assume the RGT values monotonically increase with depth.

Figure 4a and 4b shows another 2D field seismic image and its corresponding local slopes, respectively. Using only the slopes, the conventional method (Figure 4c) fails to flatten the seismic image because multiple faults exist in it and lateral waveform variations appear in its deeper section. However, our improved method still perfectly flattens most of the seismic reflections as shown in Figure 4d. Figure 4e and 4f, respectively, shows the RGT maps computed from the conventional and our improved methods, whereas the latter shows more obvious discontinuities at faults. The horizons (Figure 4h) extracted from our RGT map (Figure 4f) more accurately follow the seismic reflections than those (Figure 4g) extracted from the one (Figure 4e) computed using the conventional method.

APPLICATIONS

We apply our improved flattening method to four 3D field examples that contain many faults, missing data, and subtle channels. The application results show that our method works well in all of these cases to accurately flatten the seismic volumes and extract the horizon surfaces. By accurately flattening the seismic volumes, our method is especially helpful to reveal the buried subtle or thin channels that are significantly folded and faulted in the seismic volumes.

Example one

Figure 5 shows a 3D seismic volume that is significantly folded by the salt bodies (denoted by the red arrows) at the bottom and faulted by some large faults (dashed yellow lines) and a significant amount of smaller faults (in the layer denoted by the yellow arrow). Dealing with such complex folding and faulting structures is challenging for conventional methods of flattening and horizon interpretation. As shown in Figure 6a and 6b, the conventional flattening method can remove large structures but the flattened result is still not sufficiently accurate. Reflections are still misaligned across the large faults as shown in Figure 6a. Obvious variations of amplitude features still appear in the horizontal slice in Figure 6b, which indicates that the seismic phases are still not consistently aligned and the slice jumps among seismic peaks and troughs.

Our method yields a significantly improved result shown in Figure 6c and 6d. Reflections across large faults are accurately aligned (Figure 6c). The layer with many small faults (denoted by the yellow arrow in Figure 5) is perfectly flattened as we observe highly consistent amplitude features in the horizontal slice in Figure 6d. Based on the flattening shifts of our method, we also can compute an RGT volume (Figure 7a) and extract horizon surfaces as isosurfaces of RGT. We are able to obtain a whole volume of horizons, and Figure 7b–7d provides the different views of an arbitrary set of horizons that accurately follow reflections even across faults.

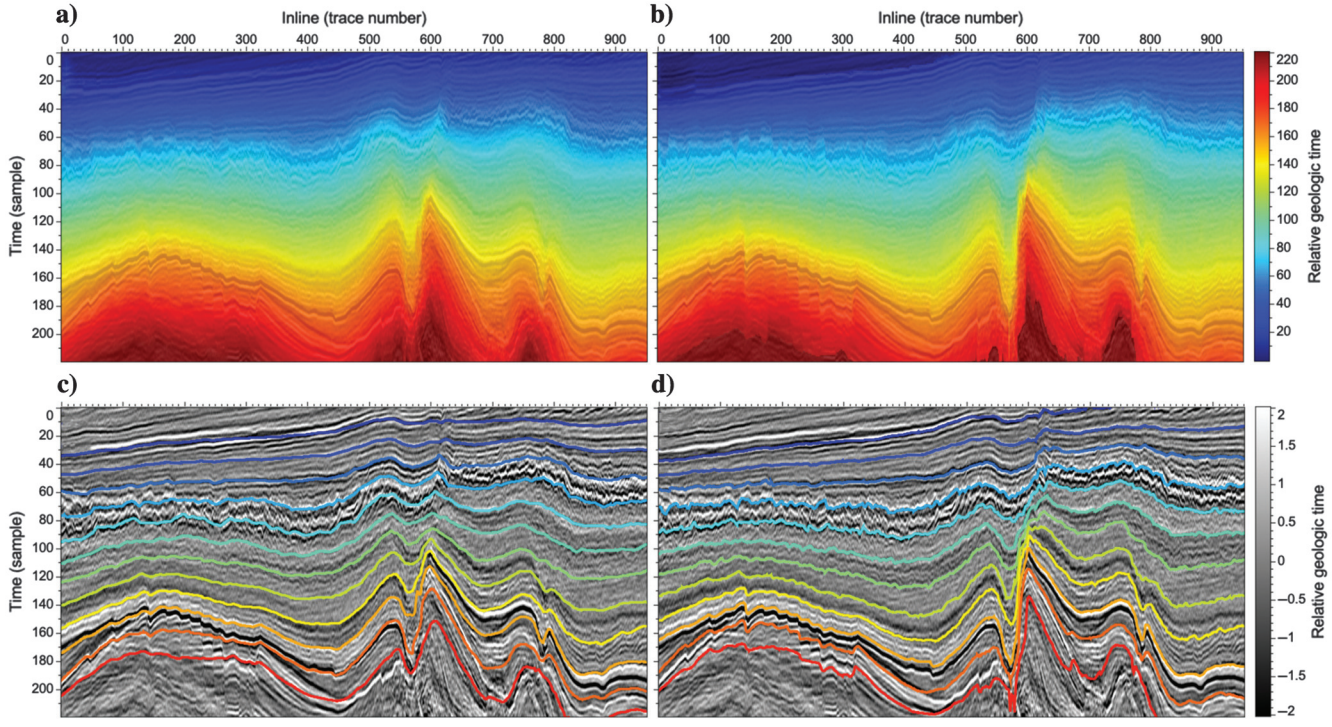

Figure 3. Based on the flattening shifts of the conventional and our improved methods, maps of RGT are computed and displayed in (a and b), respectively. From an RGT map, an arbitrary number of horizons can be automatically extracted as RGT contours. Compared with (c) the horizons extracted from (a) the conventional RGT map, (d) the ones extracted from our RGT map more accurately follow seismic structures.

Example two

Figure 8a shows another 3D field example with many faults and missing data zones which pose challenges to seismic flattening and horizon tracking. As shown in the vertical slices in Figure 8b, the conventional method using only local slopes can locally flatten the reflectors but fails to align the reflectors across faults (denoted by yellow arrows) and the missing data zones (denoted by the red arrow). In the horizontal slice in Figure 8b, we observe amplitude variations (jump from white to black) across faults (dashed yellow curves) which also indicate the misalignment of reflections across faults.

However, our method perfectly flattens (Figure 8c) the seismic reflections even across faults and missing data zones due to the use of the correlations of seismic traces. We randomly choose the traces to be correlated and some of the correlations are calculated

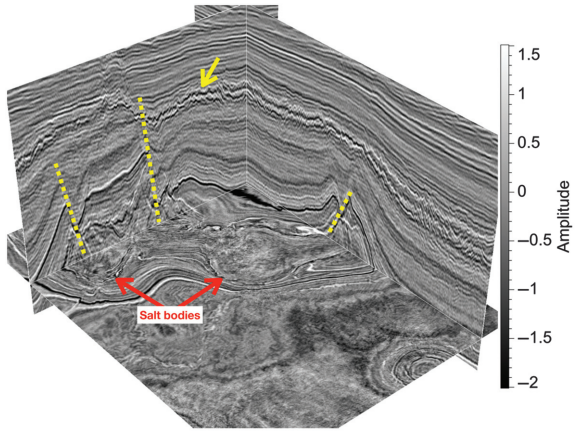

Figure 5. A 3D seismic image complicated by faults and salt bodies.

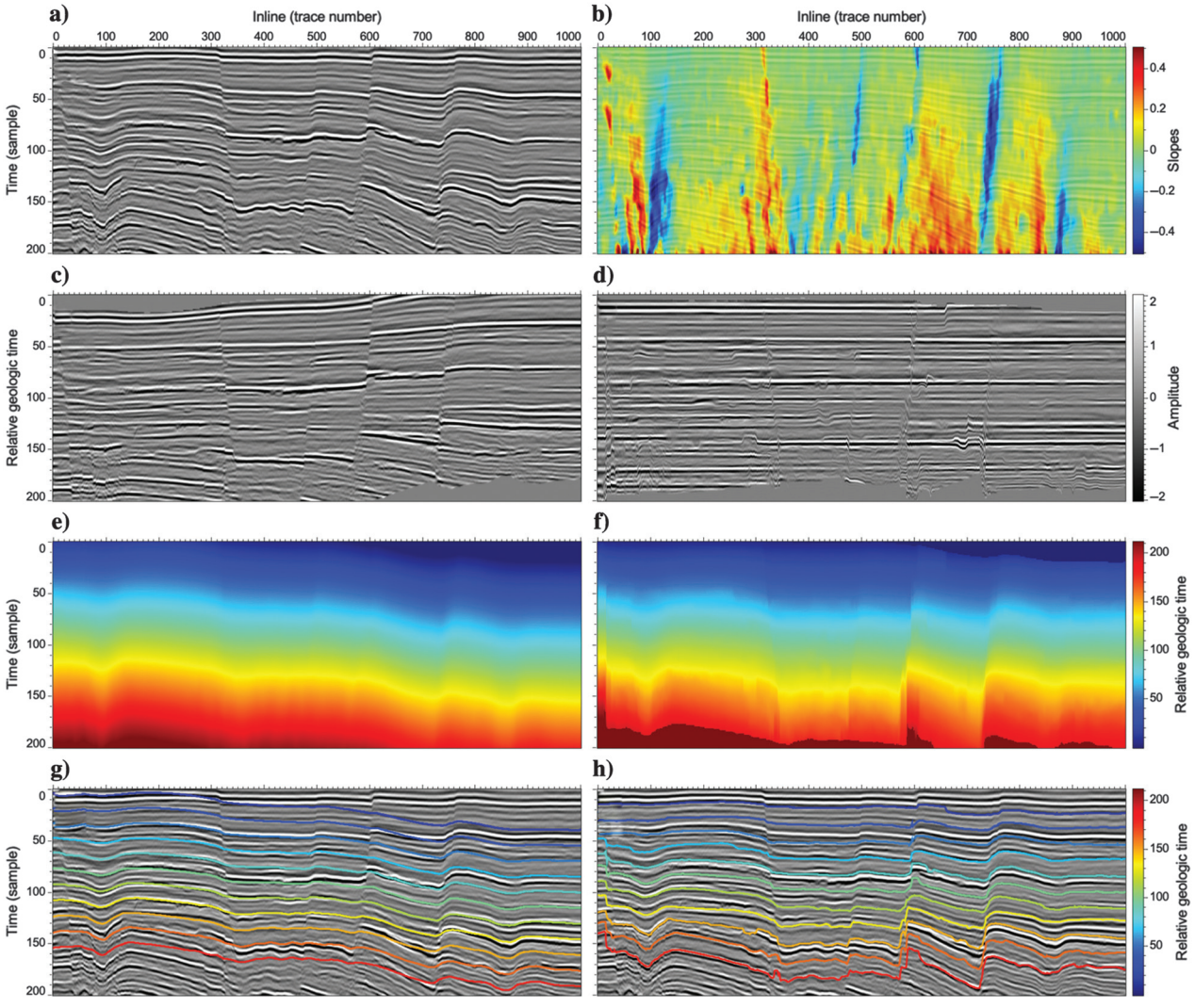

Figure 4. For (a) a seismic image complicated by faults, (b) the conventional flattening method using only reflection slopes cannot accurately (c) flatten the seismic image, especially near the faults. In contrast, (d) our improved method with slopes and seismic correlations perfectly aligns all the reflections horizontally, even across faults. (f) The RGT map computed from the flattening shifts of our method shows sharper discontinuities near the faults than (e) the one computed from the conventional shifts. (h) The horizons extracted from (f) our RGT map more accurately follow the seismic structures than (g) the ones extracted from (e) the conventional RGT map.

DOI:10.1190/geo2021-0662.1

across faults and missing data zones, which provides useful constraints to align the reflections globally. Figure 9 shows an RGT volume and an arbitrary set of horizons computed from our flattening shifts. When the shifts can accurately flatten the seismic volume, the extracted horizons will accurately follow consistent reflections as shown in Figure 9b and 9d.

Interpreting subtle stratigraphic features

In flattening a seismic volume with low-dip-angle faults, a flattening method with only vertical shifts may yield artifacts near the faults. To obtain a more reasonably flattened result in this case, we may need to first remove the faulting with nonvertical shifts (Wu et al., 2016) and then remove the folding in the unfaulted volume with our flattening method of using vertical shifts. Figure 10a shows a field seismic volume with multiple faults, from which we first extract fault surfaces and estimate fault throws (Figure 10b) for each fault surface using the method by Wu and Hale (2016). We then use the method by Wu et al. (2016) to undo the faulting (Figure 10c) in the seismic volume based on the precomputed fault surfaces and fault throws. We further remove the folding in the unfaulted volume by using the flattening method discussed in this paper.

Seismic flattening maps a seismic volume from the original domain in depth or traveltime to the Wheeler domain in geologic time, which facilitates the interpretation of stratigraphic features (such as buried channels) by horizontally slicing the flattened volume. However, to be able to clearly visualize subtle (vertically thin) channels, the flattening must be highly accurate and the alignment error needs to be less than two or even one samples. Figure 11a–11d shows the flattened results computed from the unfaulted volume (Figure 10c) by using the conventional and our methods, respectively. The flattened result by the conventional method looks relatively good in the vertical slices in Figure 11a and 11b. However, the channel in the horizontal slice in Figure 11a disappears in the area denoted by the red arrows. This is because the channel is vertically thin (with

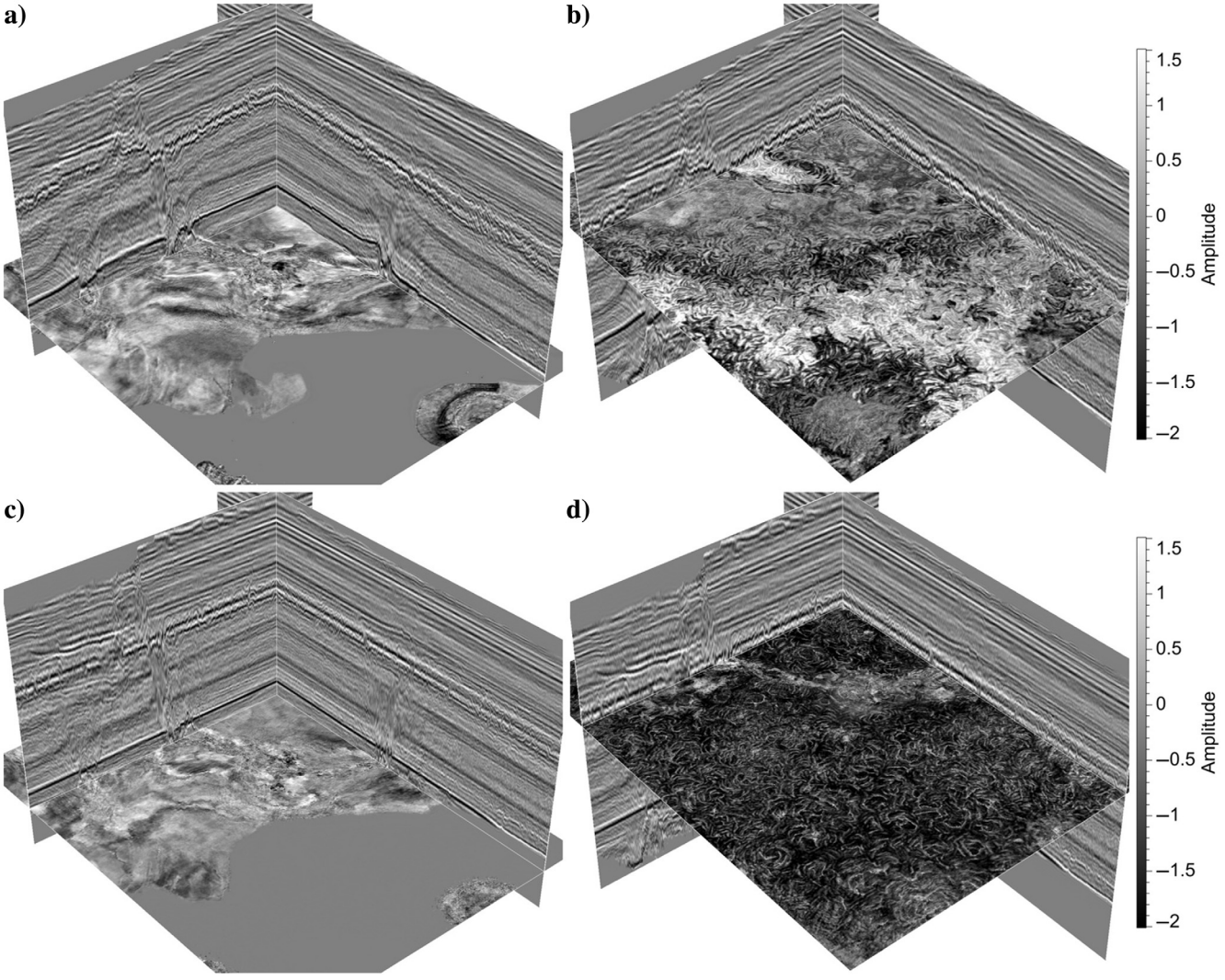

Figure 6. The 3D seismic volume (Figure 5) is flattened by using (a and b) the conventional and (c and d) our improved flattening methods, respectively. Compared with the conventional method, our method works much better to (c) flatten the seismic volume and therefore reveals more consistent amplitude features in the horizontal slice as shown in (d).

DOI:10.1190/geo2021-0662.1

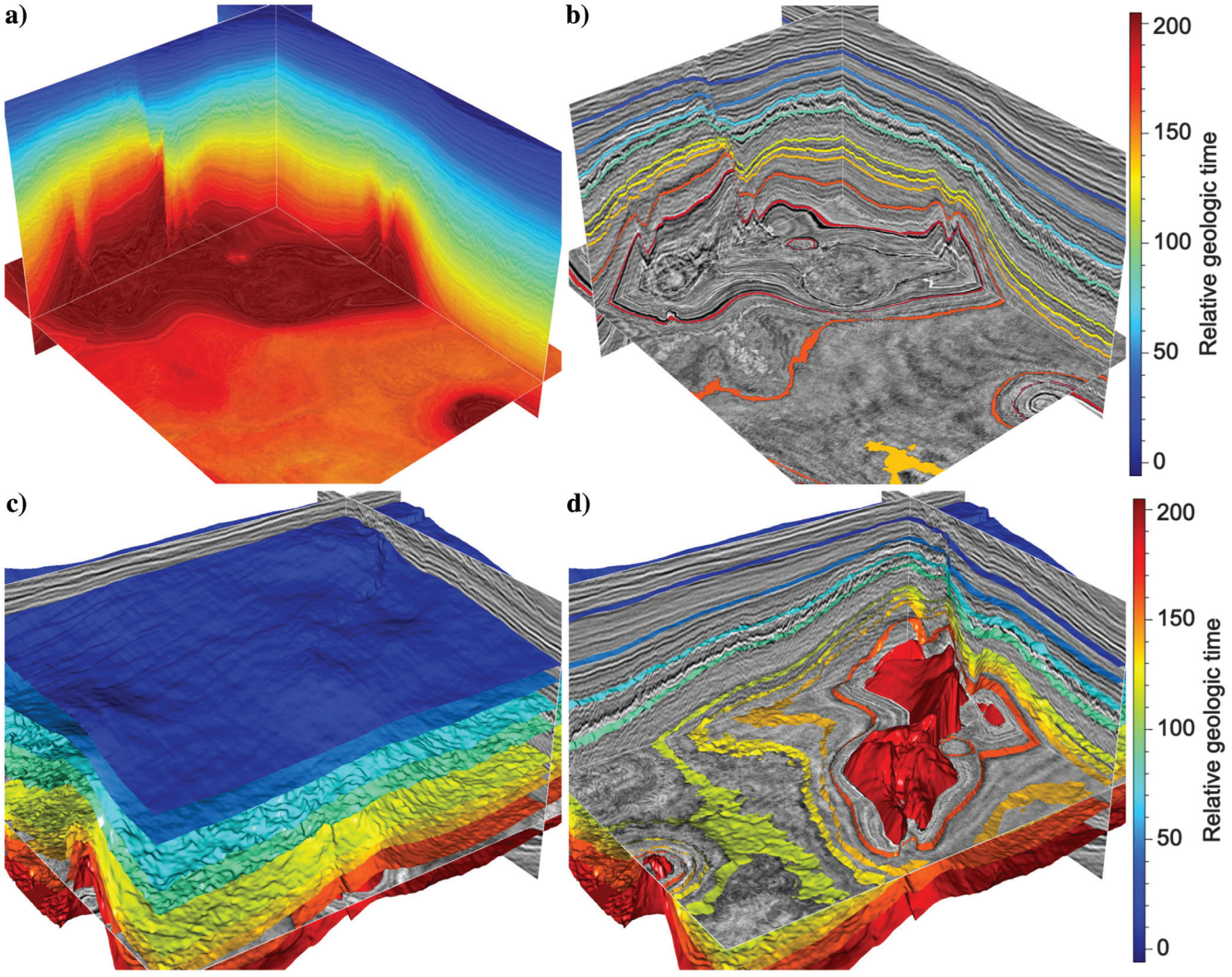

Figure 7. (a) An RGT volume and (b–d) an arbitrary number of horizons are automatically computed from the flattening shifts of our improved methods. (b) The intersection of the extracted horizons and the seismic slices. (c and d) A full and cut-away view of the extracted horizon surfaces, respectively. The extracted horizons accurately follow seismic reflections as shown in (b and d).

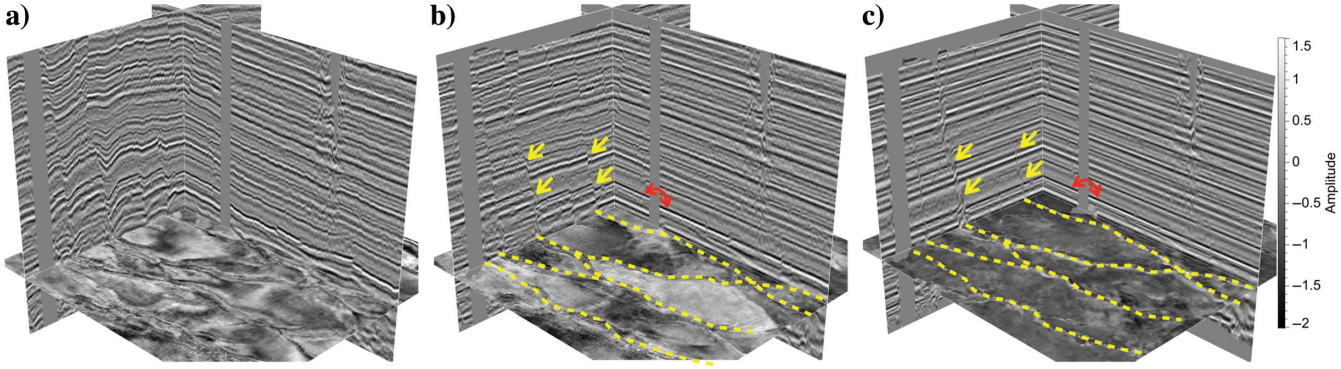

Figure 8. (a) The 3D seismic volume is flattened by using (b) the conventional and (c) our improved flattening methods, respectively. Our method is able to more accurately flatten the seismic reflections across faults (yellow arrows) and missing data zones (red arrows).

a thickness of about only one sample rate) and the flattening method is not sufficiently accurate to perfectly align the reflections corresponding to the same sedimentary strata. By using our improved method, this channel is clearly and completely revealed in the horizontal slice in Figure 11c. In Figure 11b, we observe phase changes (color jumps from black to white) of the channel denoted by the red arrow because of the misalignment using the conventional method. This phase change due to the flattening method may mislead the rock-property interpretation of the channel. From a more accurately flattened result (Figure 11d) with our improved method, this channel appears to have a consistent phase (colored by all black) in the horizontal slice.

Figure 12a shows another 3D field seismic volume with a significant amount of vertically thin channels that are dislocated by faults and bent by folding structures. Interpreting these vertically thin channels in the vertical seismic slices is challenging because of the vertical resolution limit of the seismic data. We should analyze more horizontal information following seismic horizons as suggested by Zeng and Hentz (2004) because the channels are vertically thin but often extend laterally in a large area along a stratal slice. However, uncovering the channels, especially the vertically thin ones, in the lateral space requires accurately flattening the seismic volume to the Wheeler domain where the faulting and folding structures are removed. Figure 12b–12f shows five horizontal slices of the seismic volume flattened by our method, where we observe clear and continuously trackable channels. This indicates that our flattening method accurately removes the faulting and folding structures in the seismic volume, so that the channels are horizontally

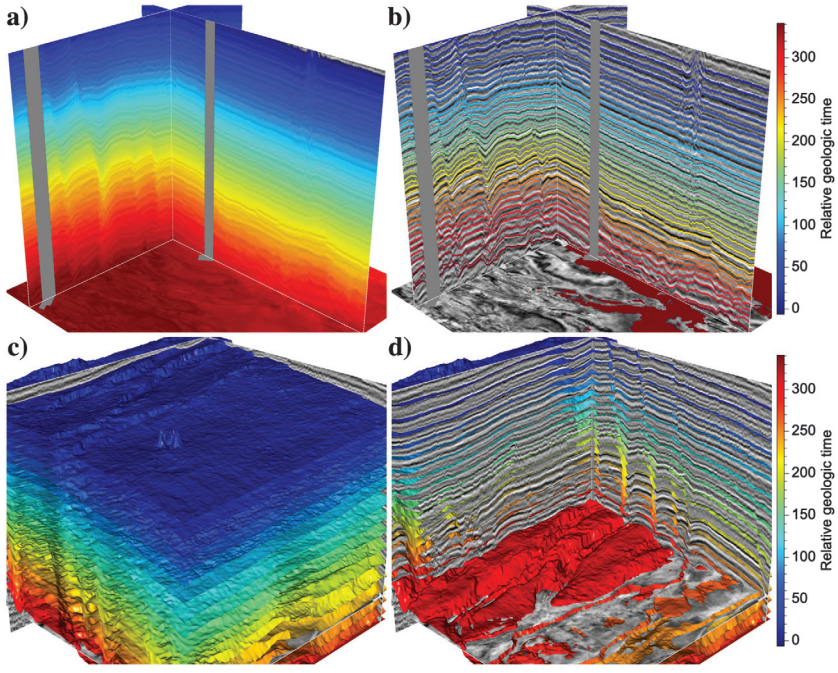

Figure 9. (a) An RGT volume and (b–d) an arbitrary number of horizons are automatically computed from the flattening shifts of our improved methods. (b) The intersection of the extracted horizons and the seismic slices. (c and d) A full and cut-away view of the extracted horizon surfaces, respectively. The extracted horizons accurately follow seismic reflections, even across faults and missing data zones, as shown in (b and d).

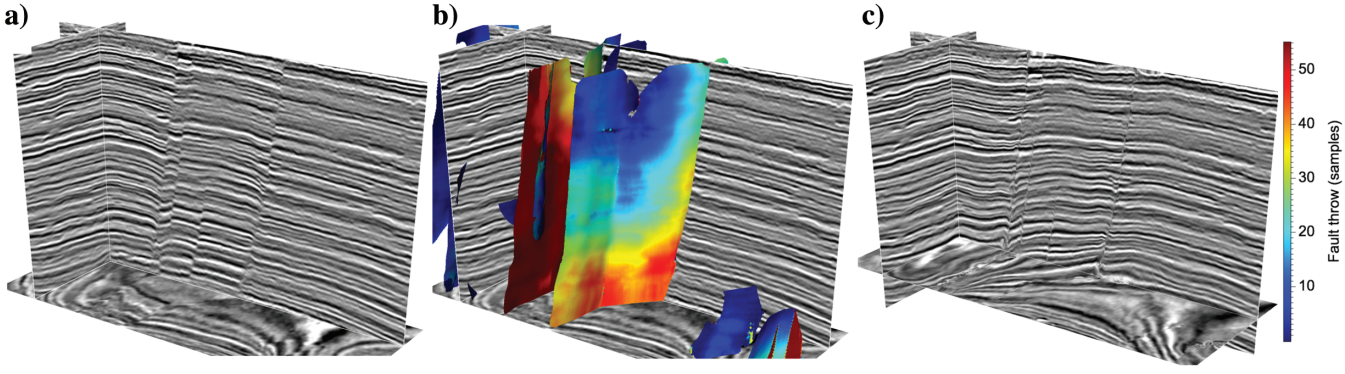

Figure 10. To avoid generating artifacts in flattening (a) a seismic volume with dipping faults, (b) we can first estimate fault throws and use them (c) to undo the faulting before flattening.

aligned (even across faults as denoted by the red arrows in Figure 12) after flattening.

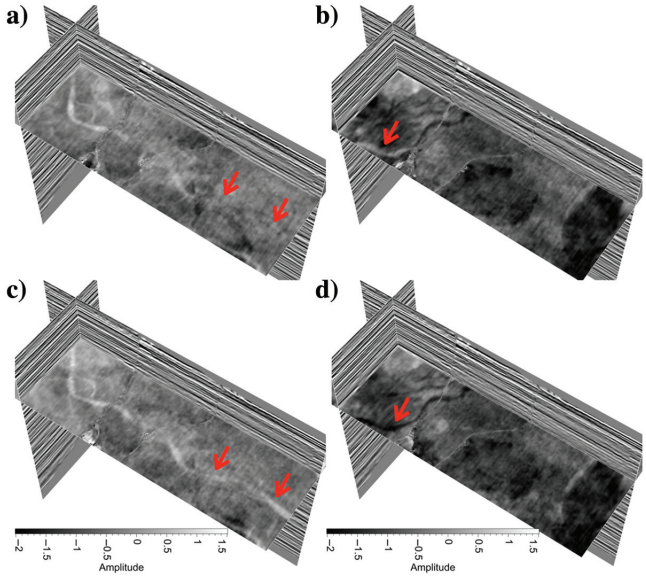

Figure 11. The unfaulted seismic volume (Figure 10c) is flattened by using (a and b) the conventional and (c and d) our improved flattening methods, respectively. By more accurately flattening the seismic volume, our method can better reveal details of the buried subtle (vertically thin) channels as denoted by red arrows in the horizontal slices.

CONCLUSION

We have proposed an improvement to the previously slope-based seismic flattening by incorporating the multigrid correlations of seismic traces. Multiple examples show that our method is more accurate than the conventional slope-based methods to horizontally align reflections in flattening a seismic volume. In addition, our method is able to accurately align seismic reflections across faults without needing to detect or remove the faults before flattening. Moreover, our method is shown to be helpful for interpreting subtle (vertically thin) channels by providing an accurate flattened volume where the seismic phases corresponding to the same horizon are consistently aligned. With the flattening shifts, we can further compute an RGT volume and obtain a whole volume of seismic horizons all at once.

Some limitations remain in our methods. One is that we compute only vertical shifts to flatten a seismic volume, which may generate artifacts near low-dip-angle faults during the flattening. One way to solve this problem is to first undo the faulting (as shown in Figure 10) in the seismic volume by using the unfaulting vector shifts and then flatten the unfaulted volume with our method. Another limitation is that our method may fail to reasonably flatten a seismic volume with unconformities where we expect to generate vertical gaps after flattening. One possible solution is to use interpreted unconformities as constraints in estimating local slopes and seismic correlations and use the unconformities as boundary control, in solving the flattening equations.

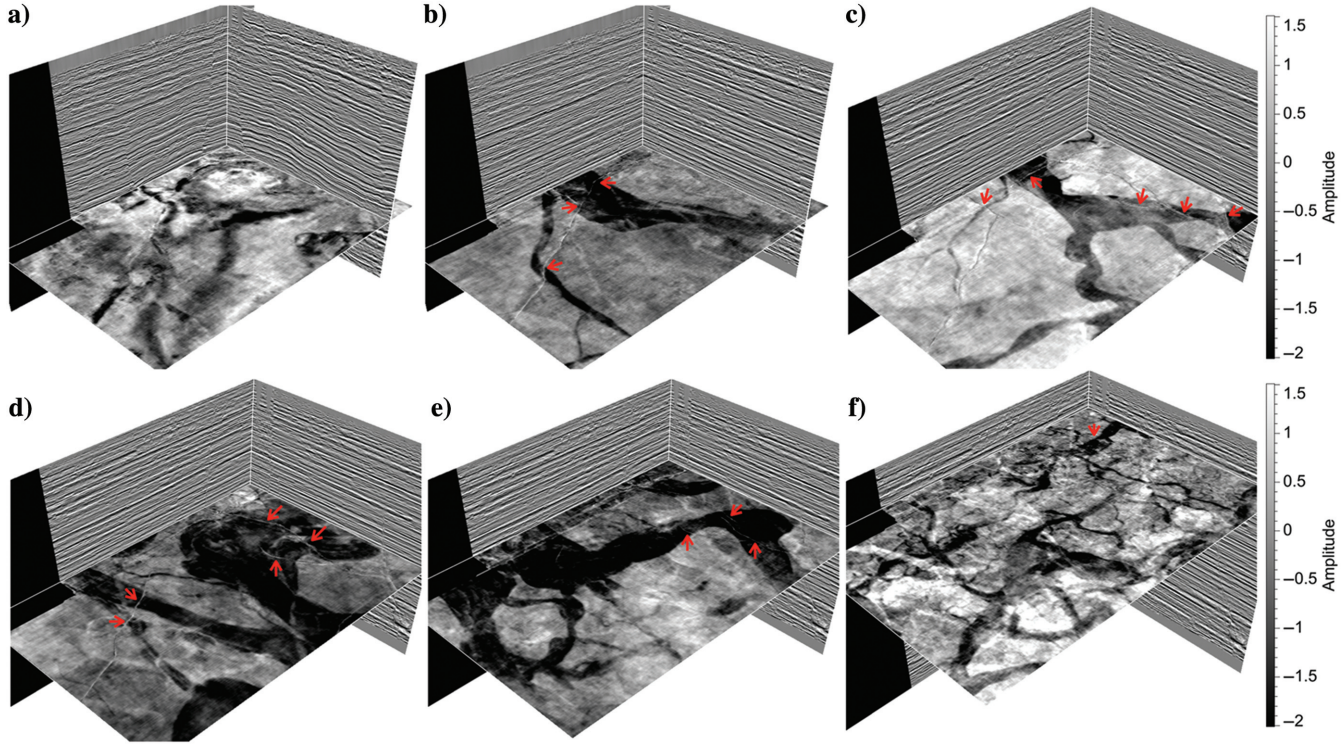

Figure 12. (a) A 3D seismic volume is accurately flattened by using our improved flattening method. (b–f) The horizontal slices of the flattened volume clearly show channel features that are invisible in the horizontal slices of the original seismic volume where the channels are significantly folded and faulted.

DOI:10.1190/geo2021-0662.1

ACKNOWLEDGMENT

This research is jointly supported by the National Science Foundation of China under grant 41974121 and the PPT Exploration and Production PLC, Bangkok, Thailand. We appreciate suggestions by the associate editor Alison Malcolm and anonymous reviewers that led to a significant revision of this paper.

DATA AND MATERIALS AVAILABILITY

Data associated with this research are available and can be obtained by contacting the corresponding author.

REFERENCES

Bakker, P., 2002, Image structure analysis for seismic interpretation: Ph.D. thesis, Delft University of Technology.

Bakker, P., L. J. van Vliet, and P. W. Verbeek, 1999, Edge preserving orientation adaptive filtering: IEEE Computer Society Conference on Computer Vision and Pattern Recognition, 535–540.

Bienati, N., and U. Spagnolini, 2001, Multidimensional wavefront estimation from differential delays: IEEE Transactions on Geoscience and Remote Sensing, **39**, 655–664, doi: 10.1109/36.911122.

de Groot, P., A. Huck, G. de Bruin, N. Hemstra, and J. Bedford, 2010, The horizon cube: A step change in seismic interpretation!: The Leading Edge, **29**, 1048–1055, doi: 10.1190/1.3485765.

Dorn, G., 2011, Interpretation workflows enabled by a domain transform: First Break, **29**, 99–108, doi: 10.3997/1365-2397.29.10.55669.

Dorn, G. A., 2013, Domain transform: A tool for imaging and interpreting geomorphology and stratigraphy in seismic volumes: The Leading Edge, **32**, 146–153, doi: 10.1190/tle32020146.1.

Fehmers, G. C., and C. F. Höcker, 2003, Fast structural interpretation with structure-oriented filtering: Geophysics, **68**, 1286–1293, doi: 10.1190/1.1598121.

Fomel, S., 2002, Applications of plane-wave destruction filters: Geophysics, **67**, 1946–1960, doi: 10.1190/1.1527095.

Fomel, S., 2010, Predictive painting of 3D seismic volumes: Geophysics, **75**, no. 4, A25–A30, doi: 10.1190/1.3453847.

Hale, D., 2009, Structure-oriented smoothing and semblance: CWP Report 635.

Hale, D., 2013, Dynamic warping of seismic images: Geophysics, **78**, no. 2, S105–S115, doi: 10.1190/geo2012-0327.1.

Labrunye, E., and C. Carn, 2015, Merging chronostratigraphic modeling and global horizon tracking: Interpretation, **3**, no. 2, SN59–SN67, doi: 10.1190/INT-2014-0130.1.

Labrunye, E., C. Winkler, C. Borgese, J.-L. Mallet, and S. Jayr, 2009, New 3D flattened space for seismic interpretation: 79th Annual International Meeting, SEG, Expanded Abstracts, 1132–1136, doi: 10.1190/1.3255052.

Lomask, J., A. Guitton, S. Fomel, J. Claerbout, and A. A. Valenciano, 2006, Flattening without picking: Geophysics, **71**, no. 4, P13–P20, doi: 10.1190/1.2210848.

Luo, S., and D. Hale, 2013, Unfaulting and unfolding 3D seismic images: Geophysics, **78**, no. 4, O45–O56, doi: 10.1190/geo2012-0350.1.

Mallet, J., 2014, Elements of mathematical sedimentary geology: The GeoChron model: EAGE Publications.

Mallet, J.-L., 2004, Space-time mathematical framework for sedimentary geology: Mathematical Geology, **36**, 1–32, doi: 10.1023/B:MATG.0000016228.75495.7c.

Mallet, J.-R., S. Jayr, and P. Neri, 2010, New modelling technology delivers consistency: First Break, **28**, 93–96, doi: 10.3997/1365-2397.28.10.41955.

Marfurt, K. J., 2006, Robust estimates of 3D reflector dip and azimuth: Geophysics, **71**, no. 4, P29–P40, doi: 10.1190/1.2213049.

Parks, D., 2010, Seismic image flattening as a linear inverse problem: Master's thesis, Colorado School of Mines.

Qayyum, F., C. Betzler, and O. Catuneanu, 2017, The Wheeler diagram, flattening theory, and time: Marine and Petroleum Geology, **86**, 1417–1430, doi: 10.1016/j.marpetgeo.2017.07.034.

Qayyum, F., C. Betzler, and O. Catuneanu, 2018, Space-time continuum in seismic stratigraphy: Principles and norms: Interpretation, **6**, no. 1, T97–T108, doi: 10.1190/INT-2017-0061.1.

Qayyum, F., P. de Groot, and N. Hemstra, 2012, Using 3D Wheeler diagrams in seismic interpretation — The HorizonCube method: First Break, **30**, 103–109, doi: 10.3997/1365-2397.30.3.56681.

Stark, T. J., 2003, Unwrapping instantaneous phase to generate a relative geologic time volume: 73rd Annual International Meeting, SEG, Expanded Abstracts, 1707–1710, doi: 10.1190/1.1844072.

Stark, T. J., 2004, Relative geologic time (age) volumes — Relating every seismic sample to a geologically reasonable horizon: The Leading Edge, **23**, 928–932, doi: 10.1190/1.1803505.

Stark, T. J., 2005, Generating a seismic Wheeler volume: 75th Annual International Meeting, SEG, Expanded Abstracts, 782–785, doi: 10.1190/1.2148275.

Vail, P. R., R. G. Todd, and J. B. Sangree, 1977, Seismic stratigraphy and global changes of sea level: Part 5. Chronostratigraphic significance of seismic reflections: Section 2. Application of seismic reflection configuration to stratigraphic interpretation, *in* C. E. Payton, ed., M 26: Seismic stratigraphy — Applications to hydrocarbon exploration: AAPG Memoirs, 99–116.

Wheeler, H. E., 1958, Time-stratigraphy: AAPG Bulletin, **42**, 1047–1063.

Wu, X., and S. Fomel, 2018, Least-squares horizons with local slopes and multigrid correlations: Geophysics, **83**, no. 4, IM29–IM40, doi: 10.1190/geo2017-0830.1.

Wu, X., and D. Hale, 2015, Horizon volumes with interpreted constraints: Geophysics, **80**, no. 2, IM21–IM33, doi: 10.1190/geo2014-0212.1.

Wu, X., and D. Hale, 2016, 3D seismic image processing for faults: Geophysics, **81**, no. 2, IM1–IM11, doi: 10.1190/geo2015-0380.1.

Wu, X., S. Luo, and D. Hale, 2016, Moving faults while unfaulting 3D seismic images: Geophysics, **81**, no. 2, IM25–IM33, doi: 10.1190/geo2015-0381.1.

Wu, X., and G. Zhong, 2012, Generating a relative geologic time volume by 3D graph-cut phase unwrapping method with horizon and unconformity constraints: Geophysics, **77**, no. 4, O21–O34, doi: 10.1190/geo2011-0351.1.

Xue, Z., X. Wu, and S. Fomel, 2018, Predictive painting across faults: Interpretation, **6**, no. 2, T449–T455, doi: 10.1190/INT-2017-0171.1.

Yu, Y., C. Kelley, and I. Mardanova, 2013, Volumetric seismic dip and azimuth estimation with 2D log-Gabor filter array: 83rd Annual International Meeting, SEG, Expanded Abstracts, 1357–1362, doi: 10.1190/segam2013-0046.1.

Zeng, H., M. M. Backus, K. T. Barrow, and N. Tyler, 1998a, Stratal slicing, Part 1: Realistic 3-D seismic model: Geophysics, **63**, 502–513, doi: 10.1190/1.1444351.

Zeng, H., S. C. Henry, and J. P. Riola, 1998b, Strata slicing, Part II: Real 3-D seismic data: Geophysics, **63**, 514–522, doi: 10.1190/1.1444352.

Zeng, H., and T. F. Hentz, 2004, High-frequency sequence stratigraphy from seismic sedimentology: Applied to Miocene, Vermilion Block 50, Tiger Shoal area, offshore Louisiana: AAPG Bulletin, **88**, 153–174, doi: 10.1306/10060303018.

Biographies and photographs of the authors are not available.